Available online at www.sciencedirect.com
ScienceDirect
Trans. Nonferrous Met. Soc. China 34(2024) 1829−1842
Transactions of Nonferrous Metals Society of China
www.tnmsc.cn

# Influence of rolling reduction on corrosion behavior of WE43 alloy

Yong CAI[1,2], Yi-peng CHEN[1,2], Hong YAN[2,3], Zhi-wei SHAN[4], Yao-zong MAO[5], Rong-shi CHEN[2]

1. School of Materials Science and Engineering, University of Science and Technology of China, Shenyang 110016, China;
2. Shi-changxu Innovation Center for Advanced Materials, Institute of Metal Research, Chinese Academy of Sciences, Shenyang 110016, China;
3. School of Materials Science and Engineering, Shandong University of Science and Technology, Qingdao 266590, China;
4. State Key Laboratory for Mechanical Behavior of Materials, Xi'an Jiaotong University, Xi'an 710049, China;
5. Shandong Key Laboratory of Advanced Aluminium Materials and Technology, Binzhou Institute of Technology, Binzhou 256606, China

Received 2 December 2022; accepted 19 May 2023

**Abstract:** The corrosion behavior of WE43 alloy with different rolling reductions (0%, 25%, 45%, and 80%) at 500 °C was investigated in 3.5 wt.% NaCl solution. The microstructure evolution of the rolled WE43 alloy was characterized in detail by means of optical microscopy (OM), transmission electron microscopy (TEM) and electron back-scattered diffraction (EBSD). The results show that with increasing reductions, basal texture is gradually enhanced and grain size gradually decreases. Only the alloy with 45% reduction exhibits dispersed dynamic precipitates. Immersion and electrochemical measurements demonstrate the decreasing order of the corrosion resistance of the rolled WE43 alloy: 45% reduction > 80% reduction > 25% reduction > 0 reduction. The best corrosion resistance of the WE43 alloy with 45% reduction is mainly related to a large number of finely dispersed precipitates, which are capable of promoting the formation of a compact corrosion product layer. The increased corrosion rate of the sample with 80% reduction is induced by the re-solution of the majority of precipitates into the matrix. The grain size, basal texture and deformation twins have a limited effect on the corrosion resistance of rolled WE43 alloy compared with the precipitates.

**Key words:** rare earth magnesium alloy; rolling reduction; precipitate; texture; grain size; corrosion hehavor

## 1 Introduction

Magnesium alloys are promising structural materials in transportation and aerospace industries because of their high specific strength and high specific stiffness [1,2]. In addition, magnesium is a beneficial element that does not disrupt metabolic processes, making it suitable for body implants [3]. The service performance of magnesium is usually improved by adding alloying elements, such as aluminum (Al), zinc (Zn), manganese (Mn), calcium (Ca) and rare earth elements (RE) [4−8]. Among all the magnesium alloys, RE magnesium alloys show the best mechanical properties [9,10]. So far, the research of high-strength and heat-resistance Mg−RE alloys has mainly focused on Mg−Gd and Mg−Y systems [9]. WE43 alloy which is a very successful commercial RE magnesium alloy can maintain excellent mechanical properties and creep resistance at 300 °C [10]. However, recent studies have shown that Mg−RE alloys have

**Corresponding author:** Hong YAN, Tel: +86-24-23915897, Fax: +86-24-23894149, E-mail: yanhong5871@163.com;
Rong-shi CHEN, Tel: +86-24-23926646, Fax: +86-24-23894149, E-mail: rschen@imr.ac.cn
DOI: 10.1016/S1003-6326(24)66510-6

lower corrosion potential than other magnesium alloys, and corrosion is a key issue in their applications [11].

Up to now, some researchers have reported the corrosion behavior of WE43 alloy in different conditions. For the effect of different corrosion solutions, FENG et al [12] found that the corrosion rate of WE43 alloy in 0.6 mol/L $Na_2SO_4$ solution is much faster than that in 0.6 mol/L NaCl solution after 7 d of immersion. For the effect of different chloride ion concentrations, PRZONDZIONO et al [13] studied the corrosion behavior of extruded WE43 alloy in 0.01−2 mol/L NaCl solution. The results showed that the corrosion rate increased with the increase of NaCl solution concentrations. For WE43 alloy in different temper conditions, the corrosion rate of the aged alloy (T6) in 3.5 wt.% NaCl solution was lower than that of solid solution-treated alloy (T4), which is caused by the interaction of the fine dispersed precipitates in T6 alloy and the growth of corrosion reaction [11]. For WE43 alloy protection against corrosion, protective coatings are available for improving the corrosion resistance of WE43 alloy, such as MAO/$TiO_2$ composite coating [14] and zinc-containing coatings [15]. Once the coatings are destroyed, the alloy substrate will be corroded rapidly and even more severely than that without coatings. Most of the previous studies focused on the corrosion behavior of WE43 alloy under different experimental conditions. Very few studies involved the intrinsic corrosion resistance of WE43 alloy matrix. The scientific strategy to improve the corrosion resistance of the alloy by adjusting the microstructure can not only save time and cost but also expand the scope of applications.

Severe plastic deformation (SPD) can effectively improve the mechanical properties and corrosion resistance of materials by refining grains and homogenizing microstructure [16]. YAN et al [17] prepared AZ80 alloy with ultra-fine grain microstructure by SPD technology, and its tensile strength reached 469 MPa and corrosion rate decreased by an order of magnitude. In fact, process parameters have great influence on the final microstructure, such as grain refinement [18,19], texture evolution [20], dynamic precipitates [21] and twins [22]. At present, most studies focus on optimizing the relationship between micro-structure and mechanical properties by changing process parameters. However, there is little work investigating the effect of microstructure caused by rolling process on the corrosion behavior of WE43 magnesium alloy.

Therefore, the rolling processes with different reductions were carried out on WE43 alloy in this work. The corrosion behavior of the rolled WE43 alloy was evaluated in 3.5 wt.% NaCl solution by electrochemical measurements as a function of the rolling reductions, i.e., 0, 25%, 45% and 80%, to clarify the scientific relationship between the rolling reductions and corrosion behavior of WE43 alloy.

## 2 Experimental

### 2.1 Sample preparation

The nominal composition of the WE43 alloy was as follows: 2.0−2.5 wt.% Nd, 3.7−4.3 wt.% Y, 2.4−4.4 wt.% rare earth elements (excluding Y, with the combined content of Nd and Gd within the range of 2.4−4.4 wt.%), 0.4−1.0 wt.% Zr, and the balanced Mg. This magnesium alloy was prepared as follows: The raw materials, such as high-purity Mg, Y, Gd, Nd and Mg−30wt.%Zr intermediate alloy, were put into a vacuum melting furnace and isothermally held at 740 °C for 120 min to ensure complete dissolution, followed by transferring into a preheated melt purification furnace, and then were transferred into a sand mold through low-pressure casting. The chemical composition of the alloy was determined to be Mg−3.71Y−1.35Gd−2.08Nd−0.58Zr (wt.%) by inductively coupled plasma-atomic emission spectrometry (ICP-AES). The plates for rolling with dimensions of 120 mm × 60 mm × 20 mm were cut from the casting ingot. Before rolling, the plates were homogenized at 525 °C for 8 h, followed by cold water quenching. After milling, rectangular plates (120 mm in length, 60 mm in width and 20 mm in height) were yielded, and then were rolled at 500 °C with various reductions (0, 25%, 45% and 80%). The unidirectional rolling process with a rolling speed of 35 m/min in a rolling machine with a roll diameter of 350 mm was conducted in this work. The plates were heated to the rolling temperature and held isothermally for 30 min before rolling. The annealing temperature after each pass was 500 °C. The specific rolling parameters were shown in Table 1. The rolled plates were quenched in cold water immediately after rolling process to maintain the rolling microstructure, avoiding the effect of static recrystallization.

**Table 1** Rolling process parameters of WE43 alloy

| Pass number | Annealing time after each pass/ min | Thickness of plates/ mm | Thickness of rolled plates/ mm | Rolling reduction/ % |
|---|---|---|---|---|
| 1 | | 20 | 15 | 25 |
| 1 | | 20 | 11 | 45 |
| 2 | 20 | 20 | 4 | 80 |

### 2.2 Microstructural characterization

The environmental scanning electron microscope (Philips XL30ESEM-FEG/EDAX) was used to observe the microstructure of the sample surface. The corrosion products were characterized by X-ray diffraction (XRD, Cu $K_{\alpha}$ radiation at 50 kV, scanning step of 0.02° and scanning range of 10°−90°). The transmission electron microscope (TEM) was used to observe the morphology of precipitates. The confocal laser scanning microscope (CLSM) was used to measure the depth of corrosion pits. The texture was obtained by electron back-scattered diffraction (EBSD). The cross-section morphologies of corrosion products were determined by scanning electron microscope−back scattered electron (SEM−BSE). The scanning Kelvin probe force microscopy (SKPFM) with a MultiMode 8 atomic force microscope was used to determine the Volta potential difference between the precipitates and the matrix.

### 2.3 Corrosion evaluation

Immersion testing was conducted to evaluate the corrosion resistance. After milling, the coupons (50 mm in length, 30 mm in width and 5 mm in height) were yielded. And then, specimens were exposed to 3.5 wt.% NaCl solution at room temperature for 24 h. The corrosion products were removed by immersing in a chromic acid solution containing 180 g/L $CrO_3$ for 5 min. Cross-section morphologies of corrosion products were observed by SEM−BSE. Corrosion rate was calculated by using mass loss method. In this work, the corrosion depth per unit time was used to characterize the corrosion rate. The commonly used unit is millimeter/year (mm/a). There were three parallel samples for all coupons with various rolling reductions.

Electrochemical tests were performed on a PARSTAT4000 electrochemistry testing system in 3.5 wt.% NaCl solution, using conventional three-electrode cell, with a saturated calomel electrode (SCE) as reference electrode, a Pt plate as counter electrode, and the samples with an exposure area of 1 $cm^2$ as working electrodes. Potentiodynamic polarization curves were recorded at a scan rate of 1 mV/s after open circuit potential (OCP) was stabilized. The voltage range was from −0.2 to 1 V (vs OCP). Before the test of electrochemical impedance spectroscopy (EIS), an initial delay of 5 min was set. The scan frequency ranged from 100 kHz to 10 mHz with a perturbation amplitude of 10 mV. The samples with immersion time of 0.5, 24 and 72 h were used for EIS measurements. The EIS data were fitted using ZSimpWin data analysis software. The electrochemical experiments were repeated three times to ensure the reproducibility.

## 3 Results

### 3.1 Microstructure

Figure 1 shows the microstructure of WE43 alloy at different rolling reductions. After homogenizing treatment at 525 °C for 8 h, the eutectic phases are completely dissolved into the Mg matrix, but there are a small amount of cubic phases distributed inside grains (Fig. 1(a)). LI et al [23] pointed out that the cubic phases in RE magnesium alloys were RE-rich phases through a mass spectrometer analysis, and they cannot be eliminated by solid solution and deformation. LI et al [24] suggested that the cubic phases had a weak effect on the corrosion behavior of magnesium alloys because of the much low volume fraction. Thus, further discussion about the effect of the cubic phases on the corrosion behavior of WE43 alloy is not conducted in this work.

When the rolling reduction is 25%, the alloy shows similar microstructure to the homogenized alloy with large grain size, and only a small amount of dynamic recrystallization occurs at grain boundaries and twin boundaries (Fig. 1(b)). For the reduction of 45% alloy (Fig. 1(c)), the volume fraction of dynamic recrystallization increases significantly, and only a small amount of large grains left. As shown in Fig. 2(a), there are also fine dispersed dynamic precipitates in this alloy, which may be due to the synergistic effect of severe plastic deformation and high temperature (500 °C). The precipitates in convex lenticular shape are dispersed on the basal plane with variations in three directions. When the rolling reduction increases to 80%, the alloy presents fully completed dynamic recrystallization, and the average grain size is about 23 μm, which is much smaller than 102 μm before rolling (Fig. 1(d)). Besides, there are also a few deformation twins. However, there are only a few precipitates at the grain boundaries and in the grains compared with the alloy with 45% reduction (Fig. 2(b)). The alloy with a reduction of 45% is obtained after one pass rolling. However, the 80% reduction alloy is obtained after two passes rolling and is annealed at 500 °C for 20 min after the first pass rolling. GUAN et al [25] studied the relationship between dynamic precipitation and recrystallization behavior of WE43 alloy. They pointed out that when the annealing temperature is higher than 490 °C, complete recrystallization will

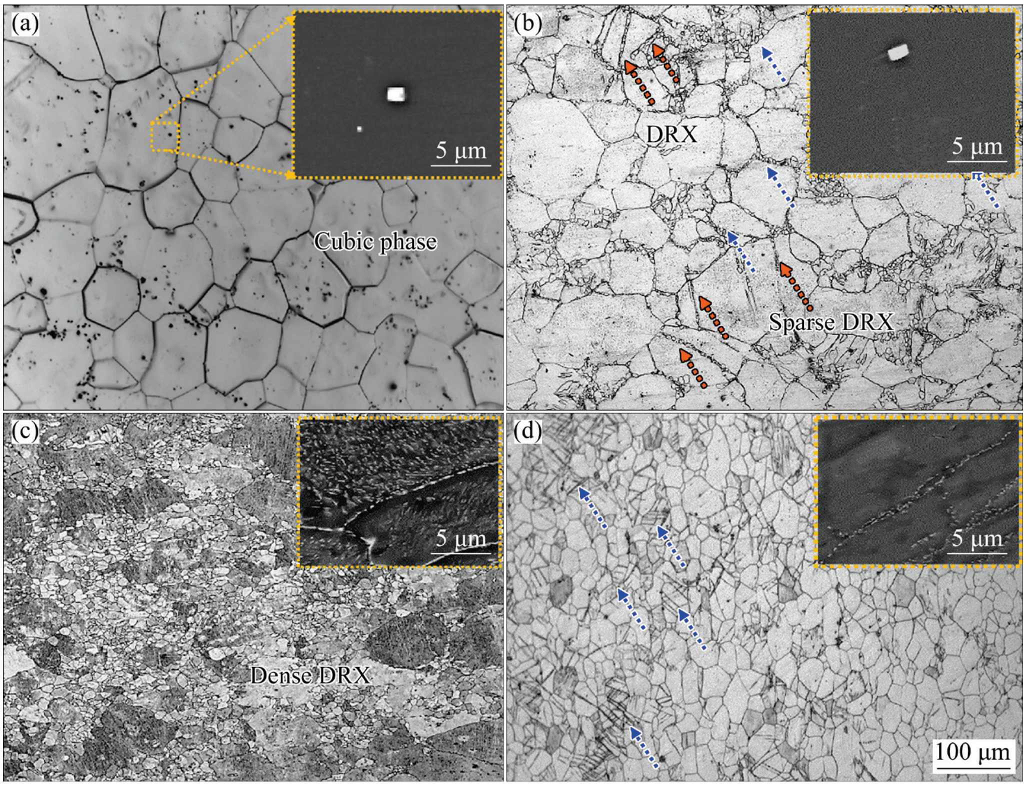


**Fig. 1** Metallographic photographs of WE43 alloy at different rolling reductions (The SEM−BSE images in the upper right corner are the corresponding high magnification images): (a) 0; (b) 25%; (c) 45%; (d) 80%

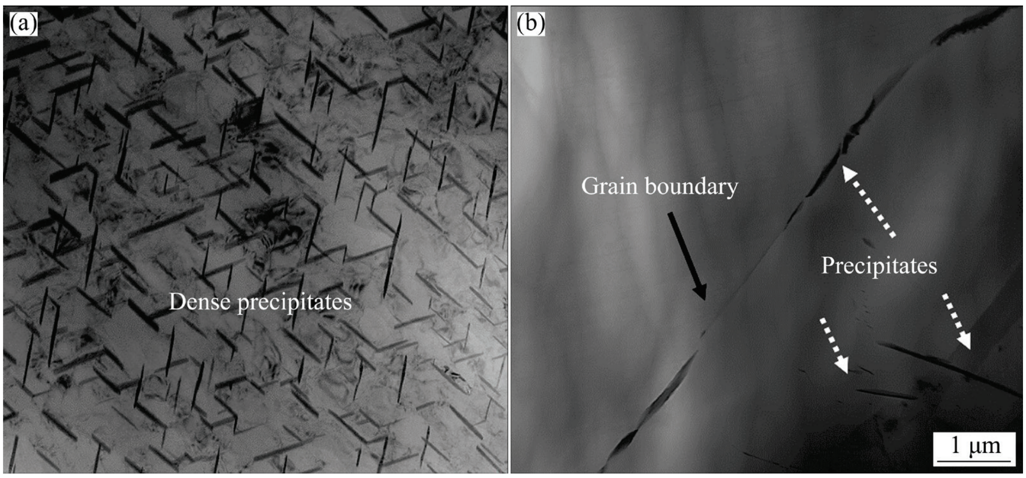


**Fig. 2** TEM images of precipitates in hot rolling WE43 alloy at rolling reductions of 45% (a) and 80% (b)

occur before dynamic precipitation. The annealing temperature of 500 °C in this work is higher than 490 °C and is close to the solution temperature of 525 °C, thus leading to the re-solution of the precipitates into the matrix and the complete recrystallization process.

Figure 3 exhibits the EBSD inverse pole figure (IPF) maps and Fig. 4 depicts the texture evolution of the solutionized WE43 alloy with different rolling reductions. The {0002} plane polar axis of the 0 reduction alloy is randomly distributed on the rolling−transverse direction plane (RD−TD), showing random texture. After rolling deformation, the alloy shows different degrees of basal texture. The position of the peak polar density of the 25% reduction alloy deflects from normal direction (ND) to transverse direction (TD) by 26.9°, and the peak density is 6.44 (Fig. 4(b)). When the rolling reduction is 45%, the deflection angle is 17.8°, and the peak density increases to 12.02 (Fig. 4(c)). As the reduction continues to increase to 80%, the {0002} polar axis is almost parallel to ND and the peak density increases to 14.84 (Fig. 4(d)). The {0002} polar axis deviating 0°−20° from ND to TD is usually considered as basal texture. The proportions of basal texture of the alloys at rolling reductions of 0, 25%, 45%, and 80% are 7.9%, 20.3%, 30.5%, and 37.8%, respectively. The texture evolution indicates that the basal planes ratio of the surface of the rolled alloy increases with the increase of the reduction. When the reduction is 80%, the rolled alloy surface exhibits the most basal planes.

### 3.2 Immersion test results

The immersion tests were used to evaluate the effect of the rolling reduction on the corrosion behavior of WE43 alloy. As shown in Fig. 5, the corrosion rate decreases rapidly from 12.5 to 1.8 mm/a with the rolling reduction increasing from 0 to 45%. When the reduction continues to increase to 80%, the corrosion rate dose not continue to decrease, but increases by 1.8 mm/a. The corrosion rate of AZ series magnesium alloys with excellent corrosion resistance is 3.52 mm/a in 3.5 wt.% NaCl solution [26]. Compared with that, the hot-rolled WE43 alloy with a corrosion rate of 1.8 mm/a exhibits excellent corrosion resistance.

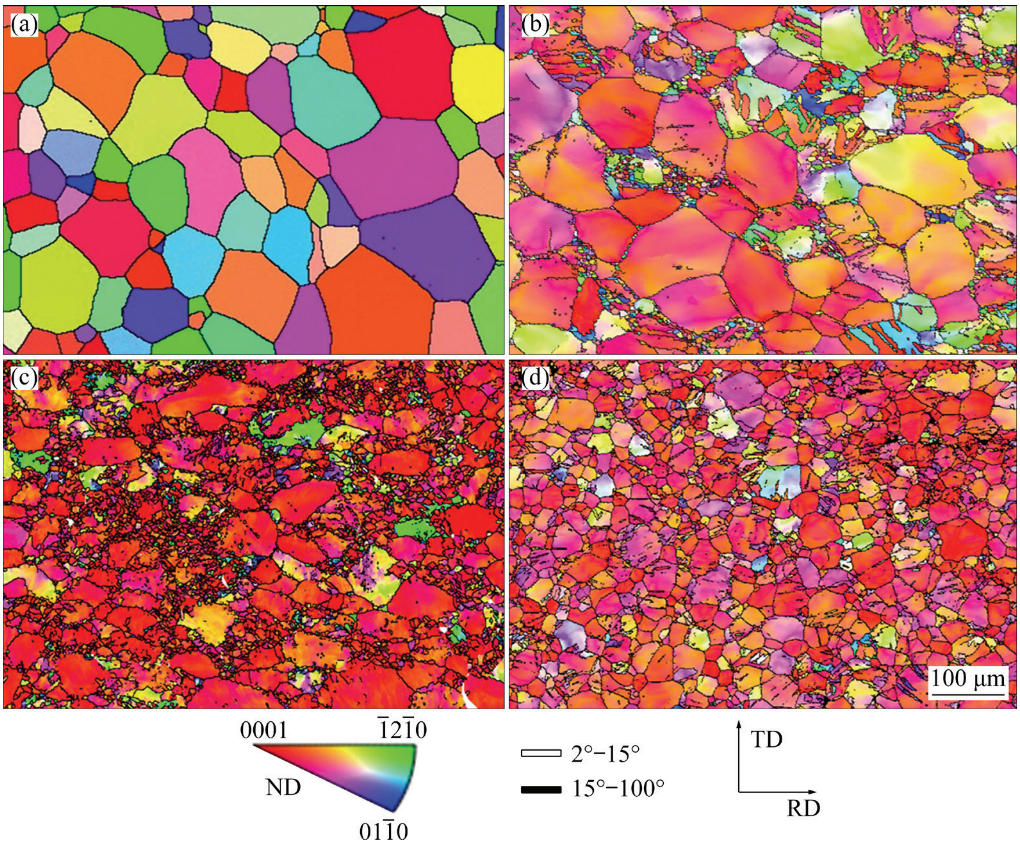


**Fig. 3** EBSD IPF maps of solutionized WE43 alloy at different rolling reductions of 0 (a), 25% (b), 45% (c), and 80% (d)

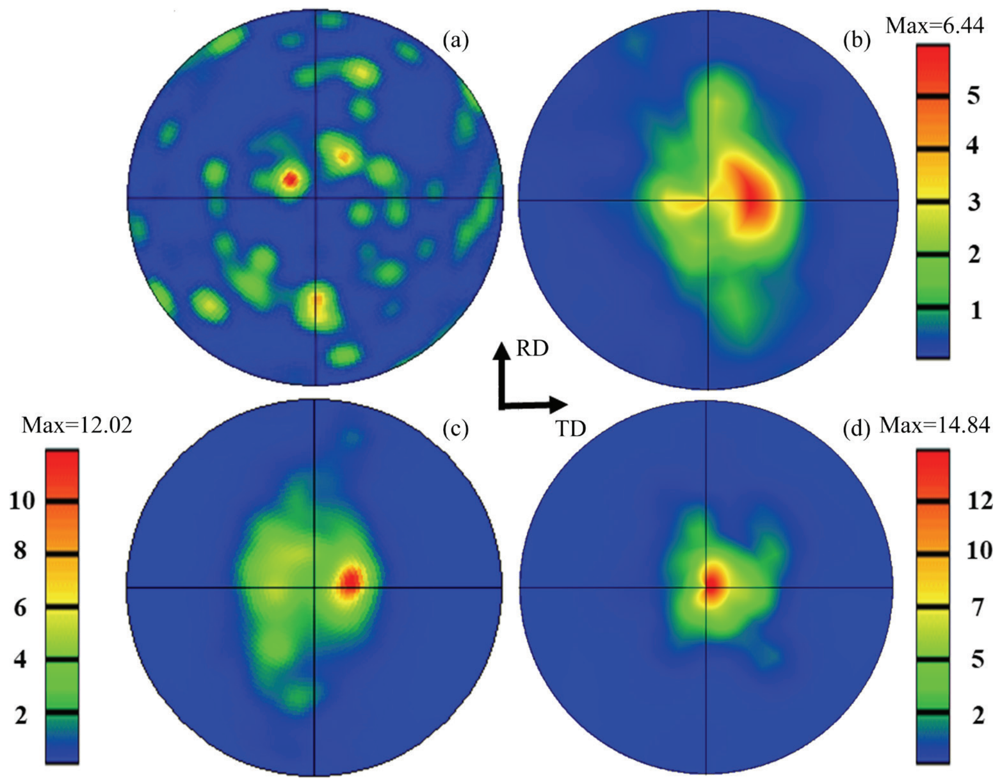


**Fig. 4** {0002} pole figures showing texture evolution in solutionized WE43 alloy at different rolling reductions of 0 (a), 25% (b), 45% (c), and 80% (d)

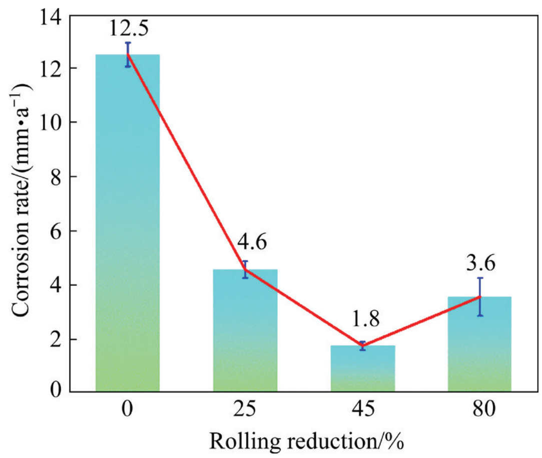


**Fig. 5** Corrosion rates of solutionized WE43 alloy at different rolling reductions of 0, 25%, 45%, and 80% after immersion tests for 24 h

Figure 6 presents the cross-section SEM−BSE images of the investigated samples after immersion in 3.5 wt.% NaCl solution for 24 h. With the reduction increasing from 0 to 45%, the thickness of the corrosion product film decreases from 10.7 to 2.9 μm. When the reduction increases from 45% to 80%, the thickness of corrosion product film increases from 2.9 to 5.4 μm, indicating that the 45% reduction alloy shows the best corrosion resistance, which is consistent with the corrosion rate change trend in Fig. 5. Moreover, it is found that numerous cracks could be observed in the corrosion product layers in the samples at 0, 25% and 80% reductions, which means that the corrosion product films are loose with limited protection. However, there are almost no cracks in the layer of the rolling 45% alloy, which corresponds to the best corrosion resistance. It should be noted that the large cracks between the film and the substrate (Fig. 6(d)) are caused by the vacuum environment during the SEM observation, rather than the characteristics of the film itself [27].

The effect of the rolling reduction on the corrosion behavior of WE43 alloy was further investigated by observing the morphology after removing corrosion products. The solutionized WE43 alloy exhibits the most serious corrosion among all samples, as the number of corrosion pits is the largest and the depth is the deepest (Figs. 7(a) and 8(a, b)). The number of corrosion pits in the alloy with 25% reduction is small, and the depth is 36 μm (Fig. 7(b) and 8(c, d)). The high-magnification SEM image shows that the dynamic recrystallization region is more seriously corroded

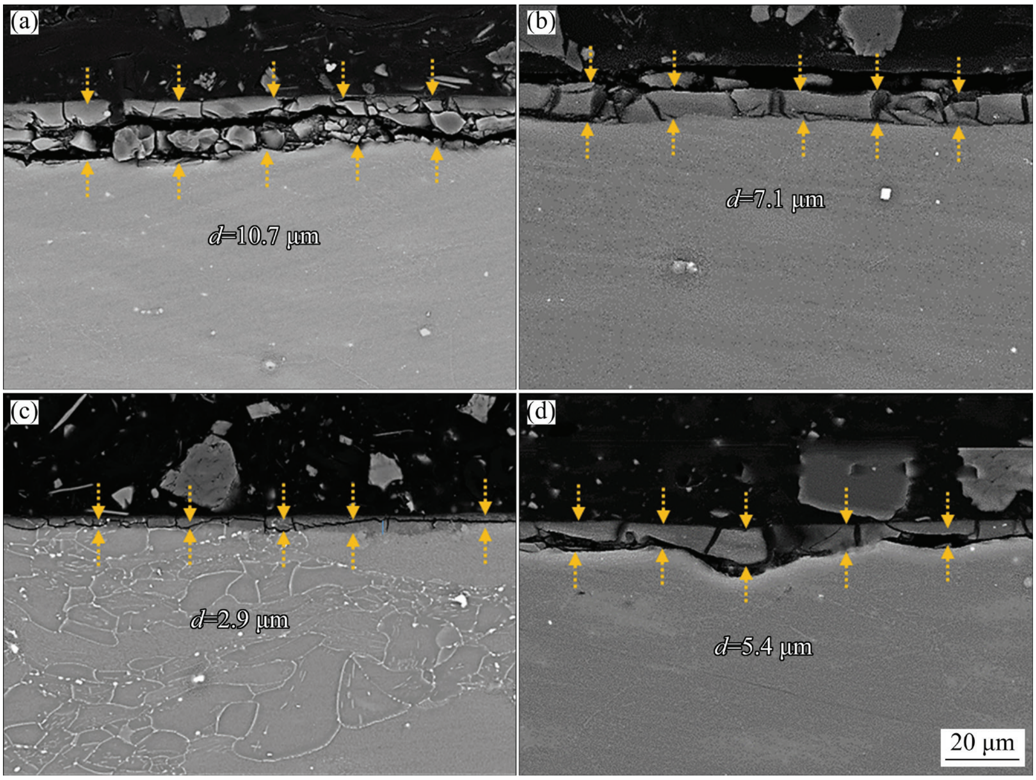


**Fig. 6** Cross-section SEM−BSE images of samples at different rolling reductions of 0 (a), 25% (b), 45% (c), and 80% (d) after immersion in 3.5 wt.% NaCl solution

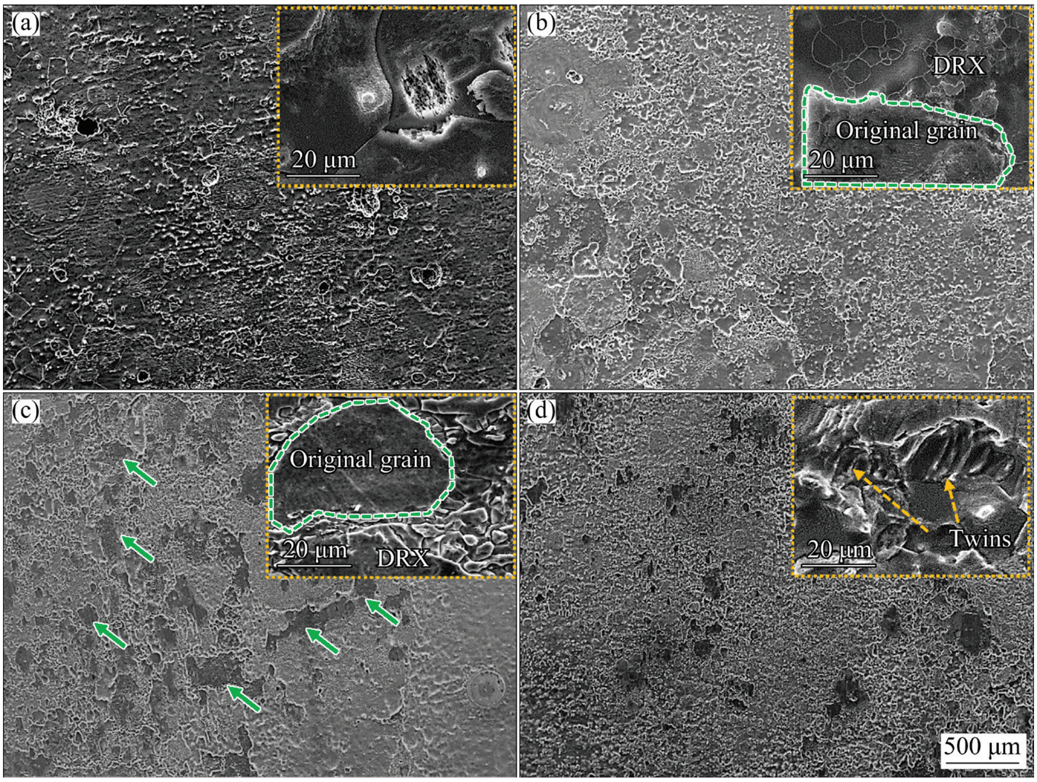


**Fig. 7** SEM images of rolled WE43 alloys at different rolling reductions immersed in 3.5 wt.% NaCl solution for 24 h after removing corrosion products (The images on upper right are corresponding high magnification images): (a) 0; (b) 25%; (c) 45%; (d) 80%

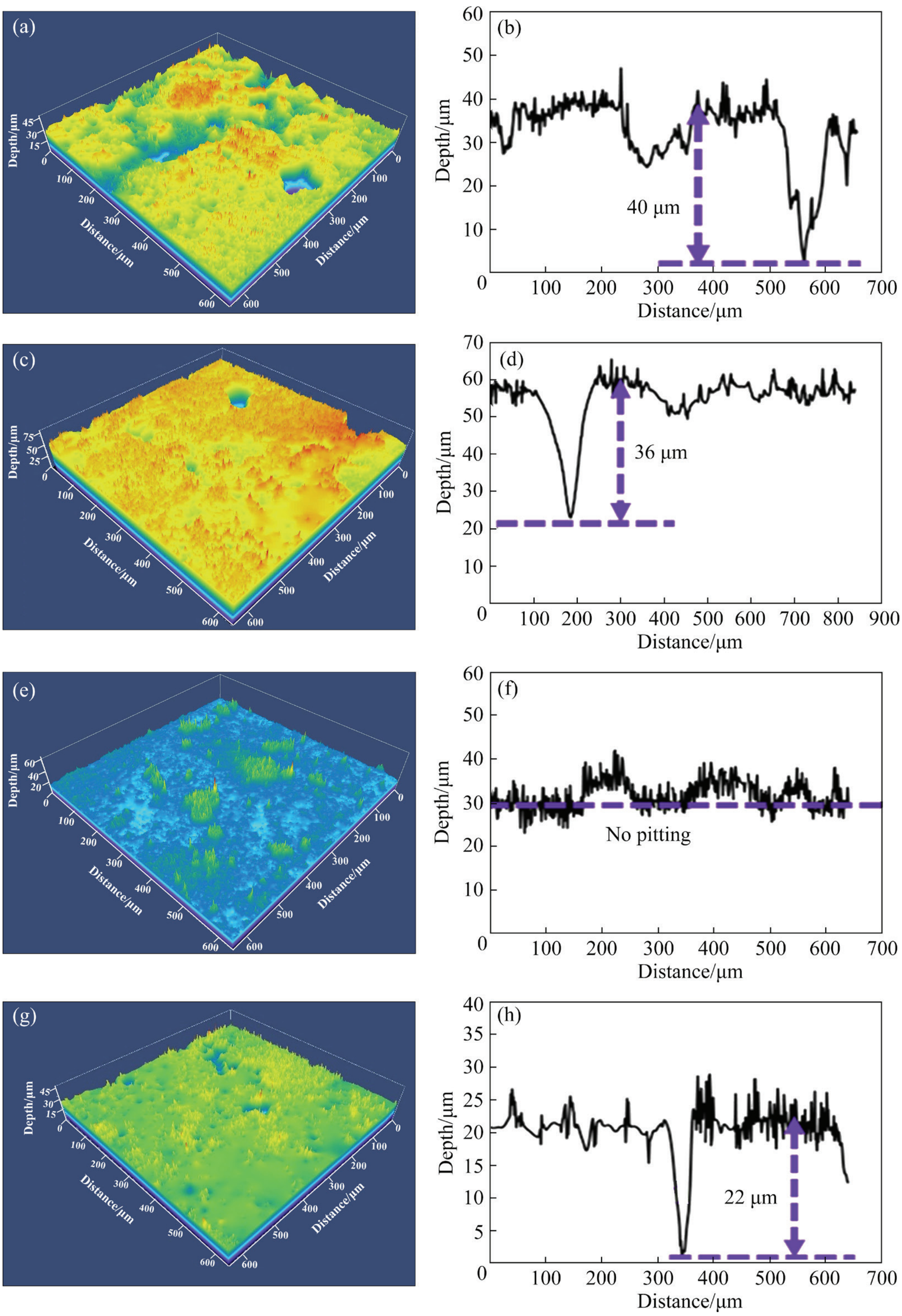


**Fig. 8** Representative 3D CLSM images and depth profiles of WE43 alloys at different rolling reductions immersed in 3.5 wt.% NaCl solution for 24 h after removing corrosion products: (a, b) 0; (c, d) 25%; (e, f) 45%; (g, h) 80%

than the original parent grains. This may be related to the grain refinement. There are a few pits in the 80% reduction alloy with a depth of about 22 μm (Figs. 7(d) and 8(g, h)). The corresponding high-magnification SEM image shows that the twinning areas are corroded obviously. At 45% reduction, the corrosion is very slight and no pits are found (Figs. 7(c) and 8(e, f)). The green arrows mark the locations where no corrosion occurs, and the non-corroded area fraction is up to 16.5%. The non-corroded matrix in the 80% reduction alloy is few and it is not observed in the 0 and 25% reduction samples.

### 3.3 Electrochemical test results

The potentiodynamic polarization curves were used to analyze the corrosion kinetics process and the protection of corrosion product film. As shown in Fig. 9, the anode branch of the no reduction alloy exhibits active dissolution characteristic, indicating that the corrosion product film is not protective. However, for the rolled alloys, there is a film breakdown potential in the anodic branches. From the drawing of partial enlargement (green box), it can be seen that the film breakdown potentials of the alloys at different reductions of 25%, 45%, and 80% are −1.63, −1.60 and −1.61 V(vs SCE), respectively. Therefore, the 45% reduction alloy has the best protective corrosion product film.

EIS is a powerful tool for quantitative analysis of the corrosion process and the failure of corrosion product film. The corrosion behavior of the WE43 alloy at different rolling reductions immersed in 3.5 wt.% NaCl solution for 0.5, 24 and 72 h is

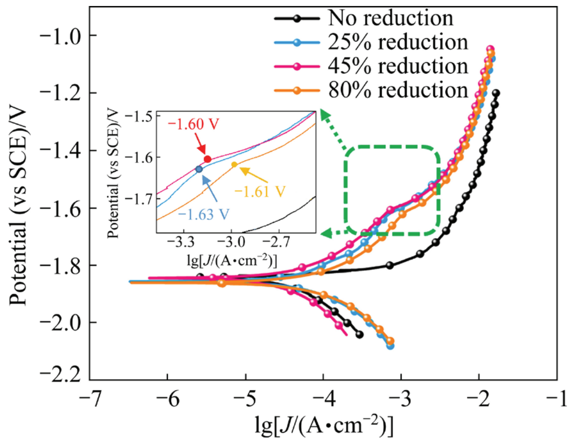


**Fig. 9** Potentiodynamic polarization curves tested in 3.5 wt.% NaCl solution for solutionized WE43 alloys with different rolling reductions

analyzed by EIS (Fig. 10). All impedance spectra in Fig. 10 contain high-frequency capacitive loops and low-frequency capacitive loops. The high-frequency capacitive loops are attributed to the magnesium oxide/hydroxide film on this alloy surface. The capacitive loops at the low frequency are related to the metallic dissolution through the

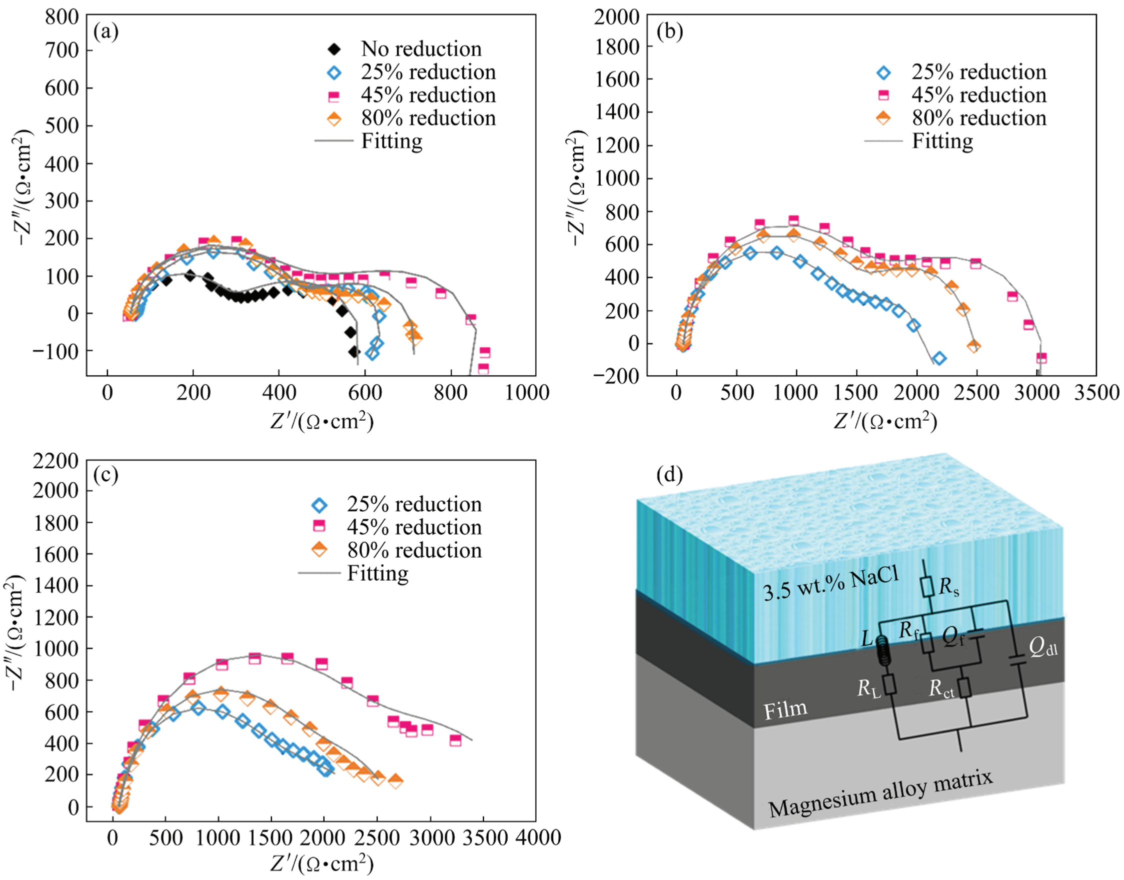


**Fig. 10** EIS Nyquist plots of solutionized WE43 alloys at different rolling reductions immersed in 3.5 wt.% NaCl solution for 0.5 h (a), 24 h (b), 72 h (c) and equivalent circuit (d)

pores and defects of this protective layer. The inductive loops are caused by local corrosion of Mg matrix.

The equivalent circuit diagram of the impedance curves is shown in Fig. 10(d), and the fitting results are shown in Table 2. $R_s$ represents the solution resistance, and $R_{ct}$ represents the charge transfer resistance which depends on the dissolution rate of the alloy contacted with the solution at the pores (cracks) of the film. $Q_{dl}$ represents double-layer capacitance. $n$, $n_{dl}$ and $n_f$ are exponents of constant phase angle elements. $Q_f$ is the film capacitance. $R_f$ represents the resistance of the alloy surface film, depending on the porosity and compactness of the surface film. $L$ and $R_L$ represent the inductance and inductive resistance of the film layer, respectively. Because of the scratches and adsorption on the actual electrode surface, the electrode process deviates from the ideal value of pure capacitance $C$. The constant phase angle element $Q$ is used to replace capacitance $C$. Figure 10(a) shows that after immersion for 0.5 h, the dimension of the capacitive loop of the no reduction alloy is the smallest, corresponding to the maximum corrosion rate. The polarization curves show that the corrosion product film on the no reduction alloy has no protection effect, which is in agreement with the EIS result. Moreover, the impedance spectra with different immersion time were not studied. With the increase of immersion time, the 45% reduction alloy shows the maximum dimension of capacitive loop. Especially after immersion for 72 h, the $R_f$ value of the 45% reduction sample is almost twice as much as that of 25% and 80% reduction alloys, which shows that the corrosion product film on the 45% reduction sample has good protection and the corrosive medium is effectively prevented from penetrating the matrix.

## 4 Discussion

The results of immersion and electrochemical tests clearly show that the corrosion resistance of the rolled WE43 alloy is significantly improved compared with that of the solid solution one, and the alloy with 45% reduction has the lowest corrosion rate. In general, grain size, precipitates, basal texture, and deformation twins have important effects on the corrosion behavior of magnesium alloys [4,24,28,29]. The corrosion behavior of WE43 alloy with different rolling reductions is discussed in terms of the microstructure induced by hot rolling.

For basal texture, the proportion of {0002} basal planes on the rolled surface increases from 7.9% to 37.8% with the increase of rolling reduction from 0 to 80% (Fig. 4). PENG et al [30] found that {0002} plane had the highest corrosion resistance compared with $\{10\bar{1}0\}$ and $\{11\bar{2}0\}$ planes by studying the potentiodynamic polarization curves of single crystal magnesium. LI et al [31] reported that {0002} plane has the highest atomic density and binding energy. And there is a negative correlation between surface energy and atomic density, indicating that the activation energy of

**Table 2** Fitting results of EIS spectra

| Immersion time/h | Reduction/% | $R_s$/ $(\Omega\cdot cm^{-2})$ | $Q_{dl}$/ $(\Omega^{-1}\cdot cm^{-2}\cdot s^n)$ | $n_{dl}$ | $R_{ct}$/ $(\Omega\cdot cm^{-2})$ | $Q_f$/ $(\Omega^{-1}\cdot cm^{-2}\cdot s^n)$ | $n_f$ | $R_f$/ $(\Omega\cdot cm^{-2})$ | $L$/ $(H\cdot cm^{-2})$ | $R_L$/ $(\Omega\cdot cm^{-2})$ |
|---|---|---|---|---|---|---|---|---|---|---|
| 0.5 | 0 | 52.07 | $3.603\times10^{-5}$ | 0.9493 | 198.2 | $4.091\times10^{-3}$ | 0.4562 | 217 | 2711 | 1000 |
| | 25 | 64.9 | $2.926\times10^{-5}$ | 0.9361 | 346.3 | $2.937\times10^{-3}$ | 0.593 | 333.7 | 1225 | 602.3 |
| | 45 | 54.88 | $2.728\times10^{-5}$ | 0.9741 | 361.6 | $2.164\times10^{-3}$ | 0.599 | 581.6 | 3353 | 100 |
| | 80 | 53.96 | $2.196\times10^{-5}$ | 0.9642 | 359.2 | $4.069\times10^{-3}$ | 0.5126 | 423.1 | 3955 | 319 |
| 24 | 25 | 54.33 | $5.667\times10^{-5}$ | 0.8949 | 2386 | $2.508\times10^{-4}$ | 0.9111 | 869.8 | 13.38 | 2404 |
| | 45 | 62 | $3.39\times10^{-5}$ | 0.9156 | 3380 | $2.14\times10^{-4}$ | 0.9156 | 1350 | 11.72 | 2951 |
| | 80 | 59.23 | $2.623\times10^{-5}$ | 0.9312 | 2421 | $2.99\times10^{-4}$ | 0.8499 | 1179 | 0.018 | 2798 |
| 72 | 25 | 66.74 | $7.65\times10^{-4}$ | 0.8665 | 3059 | $8.189\times10^{-5}$ | 0.9322 | 1498 | 20.15 | 2117 |
| | 45 | 61.39 | $4.173\times10^{-4}$ | 0.8483 | 4935.2 | $6.746\times10^{-5}$ | 0.9878 | 2168 | 35.72 | 3980 |
| | 80 | 65.29 | $3.375\times10^{-4}$ | 0.873 | 4219 | $1.266\times10^{-5}$ | 0.7919 | 1780 | 47.21 | 2515 |

surface atomic dissolution increases with the increase of atomic density. Therefore, the {0002} plane has the lowest corrosion rate. However, the alloy with 45% reduction has the lowest corrosion rate (Figs. 5 and 10), rather than the alloy with 80% which contains the most basal plane proportion. This means that texture does not play a key role in the corrosion behavior of rolled WE43 alloy in this study.

For grain size, there are a large number of recrystallized grains with size of 5−10 μm around the deformed original grains in the alloy with 45% reduction, while the alloy with 80% reduction is a fully recrystallized microstructure with grain size of 23 μm. BIRBILIS et al [32] studied the corrosion behavior of pure magnesium with different grain sizes and found that the decrease of grain size is helpful to improve the corrosion resistance. Grain refinement can compensate for the mismatch energy between the surface film and the substrate, contributing to forming a compact corrosion product film. Figure 6 depicts the increasing compactness of the corrosion product layer as follows: No reduction < 25% reduction < 80% reduction < 45% reduction, indicating that there is more important factor for the formation of dense film besides grain size.

For deformation twins, the number of twins is the most in the alloy with 80% reduction. The {0002} plane of $\{11\bar{2}0\}$ tensile twin changes from parallel to RD−TD plane to almost perpendicular to RD−TD plane. Therefore, the twinning region inside grains forms a micro-galvanic couple with the parent grain, therefore accelerating local corrosion [30]. LIU et al [33] also found that the effect of twins on the corrosion behavior of magnesium alloys depends essentially on the potential difference between different crystal faces. Therefore, it is suggested that deformation twins have a subtle effect on the corrosion behavior of WE43 alloy, just as basal texture does.

For precipitates, there are finely dispersed precipitates in the alloy with 45% reduction (Figs. 1(c) and 2(a)). According to Ref. [34], there is a potential difference between precipitates and their surrounding matrix, resulting in micro-galvanic corrosion. The Volta potential difference is determined by SKPFM technology (Fig. 11). The bias voltage of the SKPFM test is loaded on the sample. The higher the Volta potential is, the

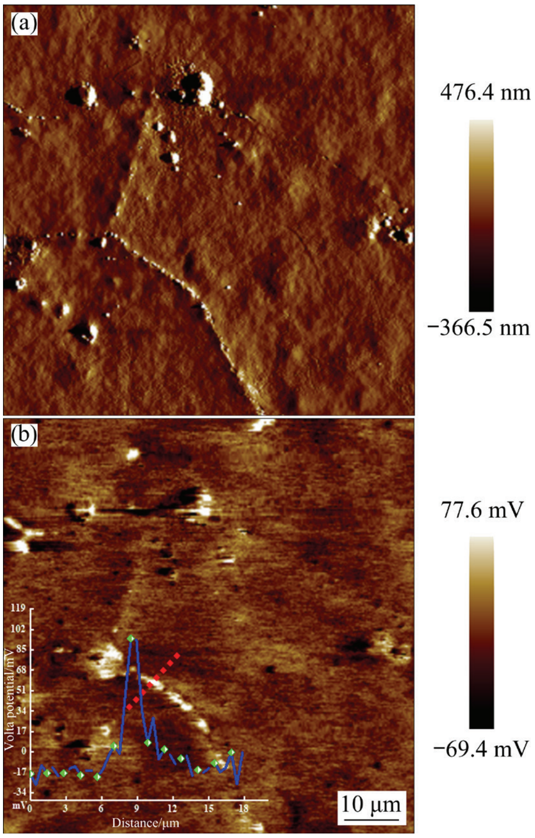


**Fig. 11** SKPFM diagrams of WE43 alloy with 45% rolling reduction: (a) Height; (b) SKPFM image and Volta potential profile of line

smaller the work function is and the higher the electrochemical activity is [4,35]. The Volta potential of the dynamic precipitates at the grain boundaries is higher than that of the matrix. The dynamic precipitates are preferentially corroded as anodes during corrosion process, slowing down the corrosion process of the matrix [4]. At the same time, the value of Pilling−Bedworth ratio (PBR) of RE oxides formed by the corrosion of precipitates is between 1 and 2 [4,36], indicating that the film has good protection. The PBR value of magnesium oxide is 0.81 [37], which could not form a dense protective film. So RE oxides can effectively improve the compactness of the corrosion product film of magnesium alloys. On the contrary, other alloys with 0, 25% and 80% reductions have pitting corrosion and cannot form dense films (Figs. 6 and 8) due to the absence of dispersed precipitates in the matrix. Electrochemical experiments (Figs. 9 and 10) prove a decreasing order of the corrosion layer compactness of the hot-rolled WE43 alloy: 45% reduction > 80% reduction > 25% reduction, which is consistent with the order of precipitation phase content. Therefore, dispersed precipitates can promote the corrosion resistance and dense corrosion product layer of WE43 alloy (Figs. 6(c), 8(e) and 9). In summary, the best corrosion resistance of the hot-rolled WE43 alloy with 45% reduction is mainly related to a large number of dispersed precipitates, which are capable of promoting a compact corrosion product layer.

## 5 Conclusions

(1) The results of immersion and electrochemical measurements demonstrate a decreasing order of the corrosion resistance of the hot-rolled WE43 alloy: 45% reduction > 80% reduction > 25% reduction > no reduction. The 45% reduction alloy shows the best corrosion resistance, and the corrosion rate is 1.8 mm/a and the pitting potential is −1.60 V (vs SCE).

(2) The best corrosion resistance of the hot-rolled WE43 alloy with 45% reduction is mainly related to a large number of fine dispersed precipitates, which are capable of promoting the formation of a compact corrosion product layer. The degraded corrosion resistance of the 80% reduction sample is caused by the re-solution of the majority of precipitates into matrix. The grain size, texture, and deformation twins have a limited effect on the corrosion resistance of the hot-rolled WE43 alloy compared with precipitates.

### CRediT authorship contribution statement

**Yong CAI:** Writing − Original draft, Writing − Review & editing, Validation, Data curation, Investigation; **Yi-peng CHEN:** Writing – Review & editing, Formal analysis, Data curation; **Hong YAN:** Writing – Review & editing, Validation; **Zhi-wei SHAN:** Validation, Formal analysis, Data curation; **Yao-zong MAO:** Validation, Formal analysis, Data curation; **Rong-shi CHEN:** Writing – Review & editing, Validation, Supervision, Resources, Project administration, Funding acquisition, Conceptualization.

### Declaration of competing interest

The authors declare that they have no known competing financial interests or personal relationships that could have appeared to influence the work reported in this paper.

### Data availability

The raw/processed data required to reproduce these findings cannot be shared at this time as the data also forms part of an ongoing study.

### Acknowledgments

This work was financially supported by the National Natural Science Foundation of China (No. 52271107), the Bintech-IMR R&D Program, China (No. GYY-JSBU-2022-012), the Natural Science Foundation of Shandong Province, China (No. ZR2021ME241), and the Natural Science Foundation of Liaoning Province, China (No. 2020-MS-004).

### References

[1] JIANG Bin, DONG Zhi-hua, ZHANG Ang, SONG Jiang-feng, PAN Fu-sheng. Recent advances in micro-alloyed wrought magnesium alloys: Theory and design [J]. Transactions of Nonferrous Metals Society of China, 2022, 32: 1741−1780.

[2] SONG Jiang-feng, CHEN Jing, XIONG Xiao-ming, PENG Xiao-dong, CHEN Dao-lun, PAN Fu-sheng. Research advances of magnesium and magnesium alloys worldwide in 2021 [J]. Journal of Magnesium and Alloys, 2022, 10: 863−898.

[3] SHIRI M, JAFARI H, SINGH R. Effect of extrusion parameters on degradation of magnesium alloys for bioimplant applications: A review [J]. Transactions of Nonferrous Metals Society of China, 2022, 32: 2787−2813.

[4] CAI Yong, YAN Hong, ZHU Ming-yu, ZHANG Kai, YI Xue-ning, CHEN Rong-shi. High-temperature oxidation behavior and corrosion behavior of high strength Mg−*x*Gd alloys with high Gd content [J]. Corrosion Science, 2021, 193: 109872.

[5] FU Y, WANG G G, HU A, LI Y, THACKER K B, WEILER J P, HU H. Formation, characteristics and control of sludge in Al-containing magnesium alloys: An overview [J]. Journal of Magnesium and Alloys, 2022, 10: 599−613.

[6] ROMZI M A F, ALIAS J, RAMLI M I M. Effect of zinc (Zn) on the microstructure and corrosion behaviour of magnesium (Mg) [J]. Materials Today: Proceedings, 2022, 48: 1873−1879.

[7] MO N, MCCARROLL I, TAN Q Y, CEGUERRA A, CAIRNEY J, DIERINGA H, HUANG Y D, JIANG B, PAN F S, BERMINGHAM M, ZHANG M X. Roles of Nd and Mn in a new creep-resistant magnesium alloy [J]. Materials Science and Engineering A, 2020, 779: 139152.

[8] HE S H, WANG C, SUN C, ZHANG Y, YAN K, JIANG J H, BAI J, XUE F, LIU H. Corrosion properties of ECAP-processed Mg−Al−Ca−Mn alloys with separate $Al_2Ca$ and $Mg_2Ca$ phases [J]. Transactions of Nonferrous Metals Society of China, 2022, 32: 2527−2540.

[9] ZHANG Jing-huai, LIU Shu-juan, WU Rui-zhi, HOU Le-gan, ZHANG Mi-lin. Recent developments in high-strength Mg−RE-based alloys: Focusing on Mg−Gd and Mg−Y systems [J]. Journal of Magnesium and Alloys, 2018, 6: 277−291.

[10] KANG Y H, WANG X X, ZHANG N, YAN H, CHEN R S. Effect of initial temper on the creep behavior of

precipitation-hardened WE43 alloy [J]. Materials Science and Engineering A, 2017, 689: 419−426.

[11] CHU Peng-Wei, MARQUIS E A. Linking the microstructure of a heat-treated WE43 Mg alloy with its corrosion behavior [J]. Corrosion Science, 2015, 101: 94−104.

[12] FENG Bao-jing, LIU Guo-nan, YANG Pei-xu, HUANG Sen-sen, QI Dong-qing, CHEN Peng, WANG Cheng-duo, DU Jiang, ZHANG Shao-jun, LIU Jin-hui. Different role of second phase in the micro-galvanic corrosion of WE43 Mg alloy in NaCl and $Na_2SO_4$ solution [J]. Journal of Magnesium and Alloys, 2022, 10: 1598−1608.

[13] PRZONDZIONO J, WALKE W, HADASIK E, SZALA J, WIECZOREK J. Corrosion resistance tests of magnesium alloy WE43 after extrusion [J]. Metalurgija, 2013, 52: 243−246.

[14] ZHANG Shi-liang, GUO Wei, LIU Ning, XIA Chao-qun, WANG Hong-shui, LIANG Chun-yong. In situ preparation of MAO/$TiO_2$ composite coating on WE43 alloy for anti-corrosion protection [J]. Vacuum, 2022, 197: 110835.

[15] ZHU Yuan-yuan, ZHANG Shu-fang, ZHAO Rong-fang, LOU Jin, ZHANG Rong-fa, HUAN Xiao-xue, ZHANG Yi-jia. Influences of $Na_2SiO_3$ and EDTA-$ZnNa_2$ concentration on properties of zinc-containing coatings on WE43 magnesium alloys [J]. Surface and Coatings Technology, 2018, 356: 108−122.

[16] SIAHSARANI A, FARAJI G. Processing and characterization of AZ91 magnesium alloys via a novel severe plastic deformation method: Hydrostatic cyclic extrusion compression (HCEC) [J]. Transactions of Nonferrous Metals Society of China, 2021, 31: 1303−1321.

[17] YAN Chang-jian, XIN Yun-chang, CHEN Xiao-Bo, XU Dao-kui, CHU P K, LIU Chao-qiang, GUAN Bo, HUANG Xiao-xu, LIU Qing. Evading strength-corrosion tradeoff in Mg alloys via dense ultrafine twins [J]. Nature Communications, 2021, 12: 4616.

[18] XU C, ZHENG M Y, WU K, WANG E D, FAN G H, XU S W, KAMADO S, LIU X D, WANG G J, LV X Y. Influence of rolling temperature on the microstructure and mechanical properties of Mg−Gd−Y−Zn−Zr alloy sheets [J]. Materials Science and Engineering A, 2013, 559: 615−622.

[19] SAVAEDI Z, MIRZADEH H, AGHDAM R M, MAHMUDI R. Thermal stability, grain growth kinetics, mechanical properties, and bio-corrosion resistance of pure Mg, ZK30, and ZEK300 alloys: A comparative study [J]. Materials Today Communications, 2022, 33: 104825.

[20] HUANG Xin-sheng, SUZUKI K, WATAZU A, SHIGEMATSU I, SAITO N. Microstructure and texture of Mg−Al−Zn alloy processed by differential speed rolling [J]. Journal of Alloys and Compounds, 2008, 457: 408−412.

[21] LU S H, WU D, CHEN R S, HAN E H. Microstructure and texture optimization by static recrystallization originating from $\{10\bar{1}2\}$ extension twins in a Mg−Gd−Y alloy [J]. Journal of Materials Science & Technology, 2020, 59: 44−60.

[22] LUO J R, GODFREY A, LIU W, LIU Q. Twinning behavior of a strongly basal textured AZ31 Mg alloy during warm rolling [J]. Acta Materialia, 2012, 60: 1986−1998.

[23] LI J L, ZHANG N, WANG X X, DI W, CHEN R S. Effect of solution treatment on the microstructure and mechanical properties of sand-cast Mg–9Gd–4Y–0.5Zr alloy [J]. Acta Metallurgica Sinica (English Letters), 2018, 31: 1−10.

[24] LI Bang-jun, SUN Jia-peng, XU Bing-qian, WU Guo-song. Corrosion behavior of Mg−5.7Gd−1.9Ag Mg alloy sheet [J]. Journal of Alloys and Compounds, 2022, 915: 165241.

[25] GUAN D K, RAINFORTH W M, GAO J H, SHARP J, WYNNE B, MA L. Individual effect of recrystallisation nucleation sites on texture weakening in a magnesium alloy: Part 1- double twins [J]. Acta Materialia, 2017, 135: 14−24.

[26] BAEK S M, LEE S Y, KIM J C, KWON J, JUNG H, LEE S, LEE K S, PARK S S. Role of trace additions of Mn and Y in improving the corrosion resistance of Mg−3Al−1Zn alloy [J]. Corrosion Science, 2021, 178: 108998.

[27] SONG G L, UNOCIC K A. The anodic surface film and hydrogen evolution on Mg [J]. Corrosion Science, 2015, 98: 758−765.

[28] XIANG Qing, JIANG Bin, ZHANG Yu-xin, CHEN Xiao-bo, SONG Jiang-feng, XU Jun-yao, FANG Liang, PAN Fu-sheng. Effect of rolling-induced microstructure on corrosion behaviour of an as-extruded Mg−5Li−1Al alloy sheet [J]. Corrosion Science, 2017, 119: 14−22.

[29] WANG Yu-jiao, ZHANG Yun, JIANG Hai-tao. Effect of grain size uniformity and crystallographic orientation on the corrosion behavior of Mg−2Zn−1Al bar [J]. Materials Characterization, 2021, 179: 111374.

[30] PENG Jin-hua, ZHANG Zhen, LONG Chang, CHEN Huan-huan, WU Yong, HUANG Ji-an, ZHOU Wei, WU Yu-cheng. Effect of crystal orientation and $\{10\bar{1}2\}$ twins on the corrosion behaviour of AZ31 magnesium alloy [J]. Journal of Alloys and Compounds, 2020, 827: 154096.

[31] LI Xin, JIANG Bin, HE Jun-jie, ZHANG Jian-yue, JIANG Zhong-tao, LIU Bo, PAN Fu-sheng. Improvement of planar isotropy, mechanical properties and corrosion resistance of extruded Mg−3Al−1Zn alloy sheet by special grain re-orientation [J]. Journal of Alloys and Compounds, 2017, 721: 106−117.

[32] BIRBILIS N, RALSTON K D, VIRTANEN S, FRASER H L, DAVIES C H J. Grain character influences on corrosion of ECAPed pure magnesium [J]. Corrosion Engineering, Science and Technology, 2010, 45: 224−230.

[33] LIU Jin-hui, HAN En-hou, SONG Ying-wei, SHAN Da-yong. Effect of twins on the corrosion behavior of Mg−5Y−7Gd−1Nd−0.5Zr Mg alloy [J]. Journal of Alloys and Compounds, 2018, 757: 356−363.

[34] COY A E, VIEJO F, SKELDON P, THOMPSON G E. Susceptibility of rare-earth−magnesium alloys to micro-galvanic corrosion [J]. Corrosion Science, 2010, 52: 3896−3906.

[35] LI C Q, XU D K, ZENG Z R, WANG B J, SHENG L Y, CHEN X B, HAN E H. Effect of volume fraction of LPSO phases on corrosion and mechanical properties of Mg−Zn−Y alloys [J]. Materials & Design, 2017, 121: 430−441.

[36] KIM Y M, YIM C D, KIM H S, YOU B S. Key factor influencing the ignition resistance of magnesium alloys at elevated temperatures [J]. Scripta Materialia, 2011, 65: 958−961.

[37] CZERWINSKI F. The oxidation behaviour of an AZ91D magnesium alloy at high temperatures [J]. Acta Materialia, 2002, 50: 2639−2654.

# 轧制压下量对 WE43 镁合金腐蚀行为的影响

蔡 勇[1,2]，陈翌鹏[1,2]，闫 宏[2,3]，单智伟[4]，毛耀宗[5]，陈荣石[2]

1. 中国科学技术大学 材料科学与工程学院，沈阳 110016；
2. 中国科学院金属研究所 师昌绪先进材料创新中心，沈阳 110016；
3. 山东科技大学 材料科学与工程学院，青岛 266590；
4. 西安交通大学 材料力学行为国家重点实验室，西安 710049；
5. 滨州工学院 山东省先进铝材料与技术重点实验室，滨州 256606

**摘 要**：在 500 ℃下制备压下量分别为 0、25%、45%和 80%的轧制 WE43 镁合金，并研究其在 3.5 wt.% NaCl 溶液中的腐蚀行为。采用光学显微镜(OM)、透射电子显微镜(TEM)和电子背散射衍射(EBSD)对轧制 WE43 合金的显微组织演变过程进行表征。结果表明，随着轧制压下量增加，合金的基面织构逐渐增强，晶粒尺寸逐渐减小。此外，仅压下量为 45%的合金中存在弥散分布的动态析出相。浸泡实验和电化学实验结果表明，轧制 WE43 合金的耐蚀性由高到底的顺序为压下量 45%＞压下量 80%＞压下量 25%＞压下量 0。压下量 45%的合金具有最好的耐蚀性，主要原因是基体中大量弥散分布的析出相能促使致密腐蚀产物膜的形成。压下量为 80%合金的腐蚀速率增加是析出相回溶至基体所致。析出相是轧制 WE43 合金腐蚀速率的主要影响因素，而晶粒尺寸、基面织构和形变孪晶是次要影响因素。

**关键词**：稀土镁合金；轧制压下量；析出相；织构；晶粒尺寸；腐蚀行为

**(Edited by Wei-ping CHEN)**